Magnetic field effects on nucleosynthesis and kilonovae from neutron star merger remnants

de Haas, S.; Bosch, P.; Mösta, P.; Curtis, S.; Schut, Nathanyel

DOI
10.1093/MNRAS/STAD2931

Publication date
2024

Document Version
Final published version

Published in
Monthly Notices of the Royal Astronomical Society

Citation for published version (APA):
de Haas, S., Bosch, P., Mösta, P., Curtis, S., & Schut, N. (2024). Magnetic field effects on nucleosynthesis and kilonovae from neutron star merger remnants. *Monthly Notices of the Royal Astronomical Society*, *527*(2), 2240-2250. https://doi.org/10.1093/MNRAS/STAD2931

Monthly Notices of the ROYAL ASTRONOMICAL SOCIETY

MNRAS **527,** 2240–2250 (2024) https://doi.org/10.1093/mnras/stad2931
Advance Access publication 2023 September 26

Magnetic field effects on nucleosynthesis and kilonovae from neutron star merger remnants

Sebastiaan de Haas,[1★] Pablo Bosch,[1] Philipp Mösta,[1,2] Sanjana Curtis [3,4] and Nathanyel Schut[1]

[1] *Gravitation Astroparticle Physics Amsterdam (GRAPPA) and Institute of High-Energy Physics, University of Amsterdam, Science Park 904, NL-1098 XH Amsterdam, the Netherlands*
[2] *Anton Pannekoek Institute for Astronomy, University of Amsterdam, Science Park 904, NL-1098 XH Amsterdam, the Netherlands*
[3] *Department of Astronomy & Astrophysics, University of Chicago, 5640 S Ellis Avenue, Chicago, IL 60637, USA*
[4] *Kavli Institute for Cosmological Physics, University of Chicago, Chicago, IL 60637, USA*

Accepted 2023 August 24. Received 2023 July 22; in original form 2022 August 15

ABSTRACT

We investigate the influence of parametric magnetic field configurations of a hypermassive neutron star (HMNS) on the outflow properties, nucleosynthesis yields, and kilonova light curves. We perform three-dimensional dynamical space–time general-relativistic magnetohydrodynamic simulations, including a neutrino leakage scheme, microphysical finite-temperature equation of state, and an initial poloidal magnetic field. We find that varying the magnetic field strength and falloff impacts the formation of magnetized winds or mildly relativistic jetted outflows, which in turn has profound effects on the outflow properties. All of the evolved configurations collapse to a black hole ∼38–40 ms after coalescence, where the ones forming jetted outflows seem more effective at redistributing angular momentum, which result in earlier collapse times. Larger mass ejecta rates and radial velocities of unbound material characterize the systems that form jetted outflows. The bolometric light curves of the kilonovae and *r*-process yields that are produced by the post-merger remnant system change considerably with different magnetic field parameters. We conclude that the magnetic field strength and falloff have robust effects on the outflow properties and electromagnetic observables. This can be particularly important as the total ejecta mass from our simulations ($\simeq 10^{-3}\,\mathrm{M}_\odot$) makes the ejecta from HMNS a compelling source to power kilonova through radioactive decay of *r*-process elements.

Key words: MHD – nuclear reactions, nucleosynthesis, abundances – methods: numerical – stars: magnetars.

1 INTRODUCTION

Multimessenger observations of GW170817 have confirmed that binary neutron star (BNS) merger remnants can launch short gamma-ray bursts (sGRB, e.g. Savchenko et al. 2017; Abbott et al. 2017a, b). Moreover, the ultraviolet (UV), optical, and (near-)infrared observations of the BNS merger show that the radioactive decay of rapid-neutron capture process (*r*-process) elements is taking place in the ejecta. (e.g. Chornock et al. 2017; Pian et al. 2017; Shappee et al. 2017; Smartt et al. 2017). Different engine models have been proposed and late-time kilonova emission and sGRB observations have placed constraints on their characterization, however magnetars were not ruled out (e.g. Margalit & Metzger 2017; Shibata et al. 2017; Metzger, Thompson & Quataert 2018). Indeed, general-relativistic magnetohydrodynamic (GRMHD) simulations of a magnetar, formed by BNS mergers, performed in Mösta et al. (2020), showed that it is a viable candidate for powering sGRBs.

r-process nucleosynthesis in the BNS merger ejecta produces large amounts of radioactive material, powering kilonova transients while producing the heaviest elements in the Universe (e.g. Goriely, Bauswein & Janka 2011; Kasen et al. 2017; Cowan et al. 2021). The extensively studied kilonova related to GW170817, AT2017gfo, displayed a two-component emission. The ‘blue’ component is associated to the early phase of the BNS merger with an emission peak in the UV/optical bands, while the ‘red’ component peaks in the (near-)infrared frequencies on the order of a few days post-merger (e.g. Shappee et al. 2017; Smartt et al. 2017). The blue component is thought to arise from lanthanide- and neutron-poor ejecta with the majority of emission originating from relatively light elements (with atomic number $A < 140$, e.g. Chornock et al. 2017; Nicholl et al. 2017). The red component would then be dominated by emission from heavily synthesized material as a result of *r*-process nucleosynthesis (nuclei with $A > 140$), therefore being lanthanide- and neutron-rich (e.g. Chornock et al. 2017; Pian et al. 2017; Tanvir et al. 2017). Furthermore, analysis of a large electromagnetic (EM) data set conducted by Villar et al. (2017) implied that for the red component, a delayed outflow from the remnant accretion disc is the most likely dominant origin of emission, in combination with an emission component from the dynamical ejecta. The origin of the blue component is not as well understood, as it has proven difficult to reproduce the inferred outflow properties with simulations (Fahlman & Fernández 2018). Among the suggested possibilities are shock-heated polar dynamical ejecta (e.g. Metzger 2017), neutrino-

★ E-mail: sebastiaan.dehaas@wur.nl

driven winds from the hypermassive neutron star (HMNS) remnant, magnetized winds from the HMNS remnant (see also Metzger et al. 2018), and remnant winds from spiral density waves (Nedora et al. 2019), where the final two seem the most promising. Furthermore, the EM data analysed by Villar et al. (2017) imply a blue kilonova component with an ejecta mass $M_{\rm ejecta}$ of $\approx 2.0 \times 10^{-2}\,{\rm M}_{\odot}$ and ejecta speed $v_{\rm ejecta} \approx 0.27c$ and a red component with $M_{\rm ejecta} \approx 1.1 \times 10^{-2}\,{\rm M}_{\odot}$ and $v_{\rm ejecta} \approx 0.14c$. However, predictions of the mass ejection rates and velocities of the blue and red components of AT2017gfo differ depending on the underlying assumptions of the model (e.g. Nicholl et al. 2017); for example, a centrally located energy deposition and a homologous expansion is assumed in Villar et al. (2017).

BNS post-merger remnants may be highly magnetized following an amplification stage as a result of magnetic instabilities, such as the Kelvin–Helmholtz instability in the shear layer between two streams of matter during the pre-merger phase (e.g. Zrake & MacFadyen 2013; Kiuchi et al. 2015). The strong magnetic field that is generated, likely, has profound effects on the remnant system. Therefore, simulations of BNS mergers increasingly account for magnetic field effects by implementing GRMHD methods (e.g. Giacomazzo, Rezzolla & Baiotti 2009; Dionysopoulou, Alic & Rezzolla 2015; Kiuchi et al. 2015; Ciolfi et al. 2019). Comparisons between GRMHD and purely general-relativistic hydrodynamic (GRHD) simulations of BNS mergers have implied robust effects of the magnetic field on outflow properties (e.g. Anderson et al. 2008; Liu et al. 2008; Kiuchi et al. 2018). Namely, it may cause the formation of mildly relativistic jetted outflows and results in considerably larger mass ejecta rates and ejecta velocities (Mösta et al. 2020).

As GRMHD and GRHD simulations of BNS mergers imply strong magnetic field effects on outflow properties, it is interesting to parametrically explore the influence of the magnetic field by varying its strength and configuration. Siegel, Ciolfi & Rezzolla (2014) investigated the latter, in the context of BNS merger remnants, using three different magnetic field geometries to determine their influence on the X-ray afterglow of the sGRB. They evolved an initially isolated axisymmetric HMNS, with a polytropic equation of state (EOS) and endowed with a magnetic field, rather than the direct outcome of a BNS merger evolution. In this work, we perform seven dynamical space–time GRMHD simulations of (post-merger) HMNS systems including a parametrized magnetic field with different field strengths and configurations, to investigate the influence of these magnetic field parameters on the HMNS outflows and kilonova. We map a snapshot of BNS post-merger data, at $t_{\rm map} = 17\,{\rm ms}$ after coalescence, from a GRHD simulation performed by Radice et al. (2018) and use it as initial data for all the simulations. We post-process the HMNS ejecta, using Lagrangian tracer particles, to compute the *r*-process yields and a spherically symmetric radiation-hydrodynamics code to compute bolometric light curves of the kilnovae. Both magnetic field parameters show profound effects on the computed outflow properties, nucleosynthesis yields, and kilonova light curves. All simulations collapse to a black hole (BH) ∼38–40 ms after coalescence of the two neutron stars. Two of the seven simulations show the emergence of mildly relativistic jetted outflows, while displaying significantly earlier BH collapse times compared to the other simulations (by ∼1.6 ms). This may imply that jetted outflows are more effective at redistributing angular momentum in the remnant system compared to magnetized winds. Furthermore, the two simulations that exhibit jetted outflow formation contain significantly larger mass ejecta rates and radial velocities of unbound material. We find that the total ejecta mass of the HMNS system is in the $2.4 \times 10^{-4}\,{\rm M}_{\odot} < M_{\rm ejecta} < 8.3 \times 10^{-3}\,{\rm M}_{\odot}$ range for all seven simulations. Finally, we show that the magnetic field has significant implications on the nucleosynthesis yields and kilonova light curves even for the weaker magnetic field range explored, thus making this a robust feature for magnetized HMNS remnants.

The paper is organized as follows. In Section 2, we describe our simulation set-up, numerical methods, and the procedure for obtaining the *r*-process yields and kilonova light curves. In Section 3.1, we discuss the various BH collapse times and outflow properties of the HMNS system, followed by the evolution of the magnetic vector field in Section 3.2. We discuss the nucleosynthesis yields and bolometric light curves of the kilonovae in Section 3.3. We summarize and discuss our conclusions in Section 4.

2 NUMERICAL METHODS AND SET-UP

The simulations performed in this work make use of the EINSTEIN TOOLKIT framework (Löffler et al. 2012), which is a publicly available infrastructure for relativistic astrophysics and gravitational physics simulations (http://einsteintoolkit.org). The code is based on multiple components, including the `Carpet` thorn that is responsible for adaptive mesh refinement (AMR; Schnetter, Hawley & Hawke 2004), the code that provides GRMHD named `GRHydro` (Mösta et al. 2014) and the MCLACHLAN module that generates the general relativity (GR) evolution (Brown et al. 2009; Reisswig et al. 2011). We use finite-volume high-resolution shock capturing methods to evolve the system in time and adopt 5th-order weighted essentially non-oscillatory (WENO5) reconstruction (Tchekhovskoy, McKinney & Narayan 2007; Reisswig et al. 2013) and the HLLE (Harten, Lax, van Leer, Einfeldt) approximate Riemann solver (Harten 1983; Einfeldt 1988). To prevent violations of the magnetic field divergence-free constraint, $\vec{\nabla} \cdot \vec{\boldsymbol{B}} = 0$, we enforce them through a constrained transport scheme. The simulations are terminated when the HMNS collapses to a BH.

2.1 Equation of state and neutrino treatment

For the simulations performed in this work we adopt a microphysical, finite-temperature EOS in tabulated form. Specifically, we use the $K_0 = 220\,{\rm MeV}$ variant of the EOS from Lattimer & Swesty (1991; where K_0 is the nuclear compression modulus), which is the so-called LS220 EOS.

The simulations include a neutrino treatment through a scheme that adopts neutrino heating and leakage approximations, based on O'Connor & Ott (2010) and Ott et al. (2013), which in turn are based on Rosswog & Liebendörfer (2003) and Ruffert, Janka & Schaefer (1996). The scheme tracks three different neutrino species; electron neutrinos $\nu_{\rm e}$, electron anti-neutrinos $\bar{\nu}_{\rm e}$ and heavy-lepton tau and muon (anti-)neutrino's, which are grouped in a single neutrino species $\nu_x = \{\nu_\mu, \nu_\tau, \bar{\nu}_\mu, \bar{\nu_\tau}\}$. By grouping these neutrino species, we assume only neutral current reactions occur. Note that this is not entirely valid, as some charged current reactions do occur, especially in the hotter regions of the NS. The following interactions are included in estimates for the neutrino energy and number emission rates; the charged-current capture processes

$$p + e^- \leftrightarrow n + \nu_{\rm e}\,, \tag{1}$$

$$n + e^+ \leftrightarrow p + \bar{\nu}_{\rm e}\,, \tag{2}$$

plasmon decay,

$$\gamma \leftrightarrow \nu + \bar{\nu}\,, \tag{3}$$

electron and positron pair annihilation/creation,

$$e^- + e^+ \leftrightarrow \nu + \bar{\nu}\,, \tag{4}$$

and nucleon–nucleon bremsstrahlung,

$$N + N \leftrightarrow N + N + \nu + \bar{\nu}\,, \tag{5}$$

where the approximate neutrino energy and number emission rates from the above processes depend on local thermodynamics and the energy-averaged optical depth. Estimates for the neutrino optical depth are based on non-local calculations, which have been implemented using a ray-by-ray approach. The scheme solves the neutrino optical depth along radial rays that cover the simulation domain using the θ and ψ directions. Trilinear interpolation is then used in spherical coordinates (r, θ, ψ) for determining the optical depth at Cartesian grid cell centres. For the simulations, 20 rays in θ are employed that cover $[0, \pi/2]$ and 40 rays in ψ, covering $[0, 2\pi]$. The rays contain 800 equidistant points each up to a distance of 120 km, after which 200 logarithmically spaced points are adopted to account for the remainder of the domain.

The approximated local neutrino heating function is based on the charged-current absorption of ν_e and $\bar{\nu}_e$, (1) and (2), and is given by

$$\mathcal{Q}^{\rm heat}_{\nu_i} = f_{\rm heat}\frac{L_{\nu_i}(r)}{4\pi r^2}\langle\epsilon^2_{\nu_i}\rangle\, S_\nu\frac{\rho}{m_{\rm n}}X_{\rm i}\left\langle\frac{1}{F_{\nu_i}}\right\rangle e^{-2\tau_{\nu_i}}\,, \tag{6}$$

where $f_{\rm heat}$ is the heating scale factor, $L_{\nu_i}(r)$ the approximate neutrino luminosity that emerges radially from below as interpolated by the ray-by-ray approach of the neutrino leakage scheme and $S_\nu = 0.25\,(1+3\alpha^2)\,\sigma_0\,\frac{1}{(m_e c^2)}$, where $\alpha = 1.23$, $\sigma_0 = 1.76 \times 10^{-44}\,{\rm cm}^{-2}$, $m_{\rm e}$ the electron mass, and c the speed of light. Additionally, $\langle\epsilon^2_{\nu_i}\rangle$ is the approximate neutrino mean-squared energy, $m_{\rm n}$ the neutron mass, $X_{\rm i}$ is the neutron or proton mass fraction for the electron neutrino's or anti-neutrinos, respectively, $\langle\frac{1}{F_{\nu_i}}\rangle$ is the mean inverse flux factor and τ_{ν_i} is the approximate neutrino optical depth. More specifically, $\langle\frac{1}{F_{\nu_i}}\rangle$ depends on neutrino radiation field details and is parametrized as a function of τ_{ν_i}, based on neutrino transport calculations from Ott et al. (2008) and given by $\langle\frac{1}{F_{\nu_i}}\rangle = 4.275\tau_{\nu_i} + 1.15$. Furthermore, the heating scale factor $f_{\rm heat}$ is a free parameter that has been set to $f_{\rm heat} = 1.05$, which is consistent with heating in core-collapse supernova simulations that adopt full neutrino transport schemes (Ott et al. 2013). The above neutrino heating function was first derived by Janka (2001). Neutrino heating is turned off in the simulations for densities $\rho < 6.18 \times 10^{10}\,{\rm g\,cm}^{-3}$, in order to maintain numerical stability. Just like for the energy deposition, we also take into account neutrino absorption, which changes the electron fraction $Y_{\rm e}$ of the fluid. This is accounted for with an additional source term in the evolution equation for the composition following O'Connor & Ott (2010). This neutrino scheme correctly captures the overall neutrino energetics up to a factor of a few when compared to a full neutrino transport scheme in core-collapse supernovae simulations (O'Connor & Ott 2010). This calibration of the leakage scheme might have an effect on its performance in an HMNS system. Additionally, not including the dependence on the energy, momentum deposition, and the annihilation of neutrino pairs in the scheme could affect our inferred composition properties of the ejecta.

2.2 Initial conditions of the simulations

The initial data are mapped from a GRHD simulation of a BNS merger by Radice et al. (2018), covering both the pre-merger phase and a small fraction of the post-merger phase. This simulation is based on the WHISKYTHC code (model LS135135M0), and evolves an equal-mass binary NS with component masses at infinity of 1.35 $M_\odot$, the same EOS, and similar neutrino treatment. The mapping of this simulation is done at a time $t_{\rm map} - t_{\rm merger} = 17$ ms, thereby avoiding transient, oscillatory effects caused by the NS remnant core in the early post-merger phase.

Five different AMR levels are implemented, varying by a factor of 2 in resolution between consecutive levels. The highest refinement level region, covering the HMNS, has a resolution $h_{\rm fine} = 185$ m, while for the coarsest region $h_{\rm coarse} = 3.55$ km. The structure of the AMR grid is made up of boxes that extend up to 177.3, 118.2, 59.1, and 29.6 km, while the outermost boundary of the simulation domain extends to a distance of ∼355 km.

At the onset of our HMNS simulations, we add a parametrized magnetic field to the simulations, which varies in strength and falloff between the different simulations. We initialize the parametrized magnetic field with the analytical prescription of the vector potential $\vec{A}$, where $\vec{B} = \nabla \times \vec{A}$, of the form

$$A_r = A_\theta = 0; \quad A_\phi = B_0\, r\, \sin(\theta)\frac{r^3_{\rm falloff}}{r^3_{\rm falloff} + r^3}\,, \tag{7}$$

where B_0 is the initial magnetic field strength and $r_{\rm falloff}$ controls the range of the magnetic field. As we add this purely poloidal, large-scale magnetic field *ad hoc*, we implicitly assume that a dynamo process is present during the pre-merger (and possibly also early post-merger) phase that is capable of producing such an ordered, strong field. Even though previous research of proto-neutron stars formed in core-collapse supernovae implies the presence of such a dynamo (e.g. Mösta et al. 2015; Raynaud et al. 2020), current BNS merger simulations are not capable of fully resolving this magnetic amplification process (e.g. Kiuchi et al. 2018).

We perform a total of seven simulations. For the first three simulations, we vary the magnetic field strength between $B_0 = \{10^{13}, 10^{14}, 10^{15}\}$ G while keeping the magnetic falloff parameter $r_{\rm falloff} = 20$ km fixed. For the next three simulations, we fix the magnetic field strength $B_0 = 10^{15}$ G while varying $r_{\rm falloff}$ between $r_{\rm falloff} = \{5, 10, 15\}$ km. For the final simulation, we change both magnetic field parameters, explicitly, $B_0 = 5 \times 10^{15}$ G and $r_{\rm falloff} = 10$ km. We list the values of the magnetic field parameters of the seven simulations in Table 1, and include corresponding nomenclature for the simulations.

Table 1. Initial conditions of the various magnetic fields that have been adopted during the seven performed simulations of this work. The parameter B_0 controls the magnetic field strength, while $r_{\rm falloff}$ is responsible for the range the magnetic field. For the mathematical form of the vector potential of the magnetic field, see equation (7).

Simulation name	B_0 (G)	$r_{\rm falloff}$ (km)
B15-r20	10^{15}	20
B14-r20	10^{14}	20
B13-r20	10^{13}	20
B15-r5	10^{15}	5
B15-r10	10^{15}	10
B15-r15	10^{15}	15
B5-15-r10	5×10^{15}	10

2.3 Nucleosynthesis and kilonova analysis

To calculate the nucleosynthesis yields, we use Lagrangian tracer particles to determine the encountered neutrino luminosities and thermodynamic quantities of the merger outflows. The tracer particles

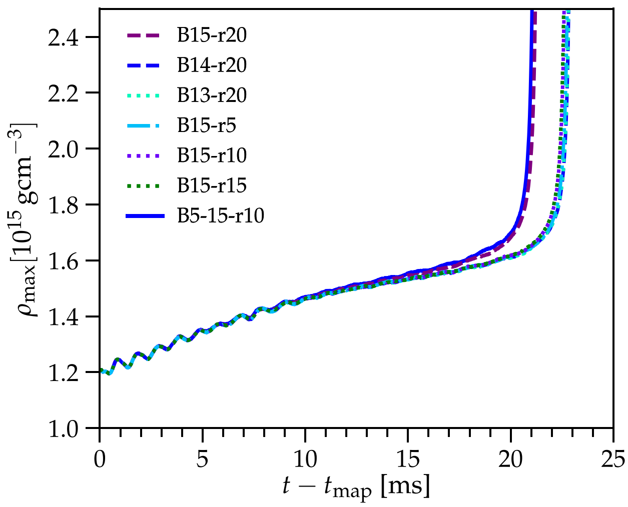

Figure 1. The maximum density $\rho_{\rm max}$ as a function of time for all simulations, where $t_{\rm map} = 17$ ms after coalescence. Simulations B15-r20 and B5-15-r10 display earlier BH collapse times of ∼21.3 ms compared to the other simulations, which collapse after ∼22.9 ms.

are spaced uniformly and we extract the corresponding quantities once the tracers reach a distance of $r = 150\,{\rm M}_\odot$. We determine the composition of the merger ejecta by post-processing the tracers using the nuclear reaction network `SkyNet` (Lippuner & Roberts 2017). REACLIB is used to obtain the forward strong rates, nuclear masses, partition functions, and part of the weak rates (Cyburt et al. 2010). The remaining weak rates are taken from Fuller, Fowler & Newman (1982), Oda et al. (1994), or Langanke & Martínez-Pinedo (2000).

Note that we adopt an approximate neutrino leakage scheme in the simulations, while the ejecta composition depends sensitively on the neutrino transport performed by this scheme. This causes uncertainties in our predictions of $Y_{\rm e}$ distributions and r-process abundances. These uncertainties have been investigated by Curtis et al. (2022), where various neutrino luminosities have been adopted to determine its influence on the r-process abundances and $Y_{\rm e}$ distributions. They conclude that the r-process production of heavy elements is reduced by up to a factor of ∼10 when comparing the two most extreme cases that bracket the entire adopted parameter space.

In order to compute the luminosity of the kilonova on a time-scale of days, we use a modification of SNEC (SuperNova Explosion Code) Morozova et al. (2015), which is a one-dimensional Lagrangian equilibrium-diffusion radiation hydrodynamics code that can simulate the evolution of merger outflows and consequent kilonova emission. Modifications to SNEC are implemented to account for kilonova as opposed to supernova modelling, such as the nickel heating term which is replaced by radioactive heating from r-process nuclei. We follow the same procedure as Curtis et al. (2022), where more details on the modifications and methods of the kilonova modelling and on the post-processed nucleosynthesis can be found.

3 RESULTS

3.1 Black hole collapse and outflow properties

In Fig. 1, we show the maximum density $\rho_{\rm max}$ as a function of time for all simulations. Simulations B15-r20 and B5-15-r10 collapse to a BH after ∼21.3 ms, while the other simulations show an on-average increased collapse time of ∼1.6 ms at ∼22.9 ms (all simulations display slight differences in the exact collapse times). The significant difference in collapse time of ∼1.6 ms between these two groups of simulations may be explained by the stronger magnetic fields and formation of mildly relativistic jetted outflows for these two simulations, which could cause a more efficient redistribution of angular momentum. Even though all simulations launch magnetized winds along the rotation axis of the HMNS remnant (Thompson, Chang & Quataert 2004), only for the two aforementioned simulations is the magnetic field powerful enough to collimate part of the outflow from the HMNS into jetted outflows.

In order to evaluate the properties of unbound material exclusively, we calculate the material's Bernoulli criterion $-hu_{\rm t} > 1$ (Kastaun & Galeazzi 2015; Foucart et al. 2021), where $h = (1 + \epsilon + p + \frac{b^2}{2})/\rho$ is the fluid's relativistic enthalpy and $u_{\rm t}$ the time component of the fluid four-velocity.[1] If the Bernoulli criterion is satisfied, the corresponding material is unbound. In the upper row of Fig. 2, we show histograms of the velocity's radial component $v^{\rm r}$ of unbound material with corresponding ejecta mass $M_{\rm ejecta}$ for simulations B13-r20, B14-r20, and B15-r20 at $t - t_{\rm map} = 5$ and 20 ms. In addition, we show the evolution of the sphere-averaged mass ejecta rates $\dot{M}_{\rm ejecta}$ as a function of time for the same simulations, which are computed using

$$\dot{M}_{\rm ejecta} = \int_{r_1}^{r_2} \sqrt{g}\rho W v^{\rm r} {\rm d}V \frac{1}{(r_2 - r_1)}\,, \tag{8}$$

with $r_1 = 44.3$ km and $r_2 = 192.1$ km. Material is only included in this computation if the Bernoulli criterion is satisfied. We show B15-r20 (which is almost identical to B15-low in Mösta et al. 2020) as a reference case in black.[2]

For the $v^{\rm r}$ evolution at $t - t_{\rm map} = 5$ ms, B13-r20 and B14-r20 display very similar $v^{\rm r}$ profiles with $v^{\rm r} < 0.3c$. Simulation B15-r20 contains significantly larger ejecta masses for nearly all $v^{\rm r}$, while also displaying ejecta in the $0.3c < v^{\rm r} < 0.5c$ regime. By $t - t_{\rm map} = 20$ ms, the ejecta mass across all velocity bins have decreased significantly for all simulations. The $v^{\rm r}$ profile of B14-r20 exhibits larger ejecta masses in the $v^{\rm r} > 0.2c$ range while B13-r20 loses all of its ejecta in this velocity regime. For B15-r20, the mass ejecta peak has shifted to significantly lower velocities ($v^{\rm r} \simeq 0.08c$).

Simulation B15-r20 shows considerably larger $\dot{M}_{\rm ejecta}$ during its evolution compared to B14-r20 and B13-r20. Simulations B14-r20 and B13-r20 exhibit very similar $\dot{M}_{\rm ejecta}$ patterns, while also displaying two short peaks at $t - t_{\rm map} \sim 6$ ms and $t - t_{\rm map} \sim 7.5$ ms. These $\dot{M}_{\rm ejecta}$ peaks are slightly enhanced for simulation B13-r20 compared to B14-r20, although the latter does generally display larger $\dot{M}_{\rm ejecta}$ values compared to the former.

In the lower row of Fig. 2, we show $v^{\rm r}$ histograms of unbound material with corresponding ejecta masses for simulations with varying $r_{\rm falloff}$. These are B15-r5, B15-r10, B15-r15, B15-r20, and B5-15-r10. At $t - t_{\rm map} = 5$ ms, all displayed simulations exhibit apparent differences in $v^{\rm r}$ profiles, where especially B5-15-r10 contains large amounts of high-velocity ejecta with $0.3c < v^{\rm r} < 0.66c$ while B15-r20 also shows some high-velocity outflows with $0.3c < v^{\rm r} < 0.52c$. Simulations B15-r10 and B15-r15 exhibit less high-velocity ejecta with $0.3c < v^{\rm r} < 0.42c$ and $0.3c < v^{\rm r} < 0.48c$,

[1] In general, Bernoulli's criterion is written as $-hu_{\rm t} > h_\infty$ (Foucart et al. 2021). For the LS220 equation of state, used in this work, $h_\infty \sim 1$ for $Y_{\rm e} = 0.44$.

[2] We modified how tracer particles record neutrino luminosities in low-density regions.

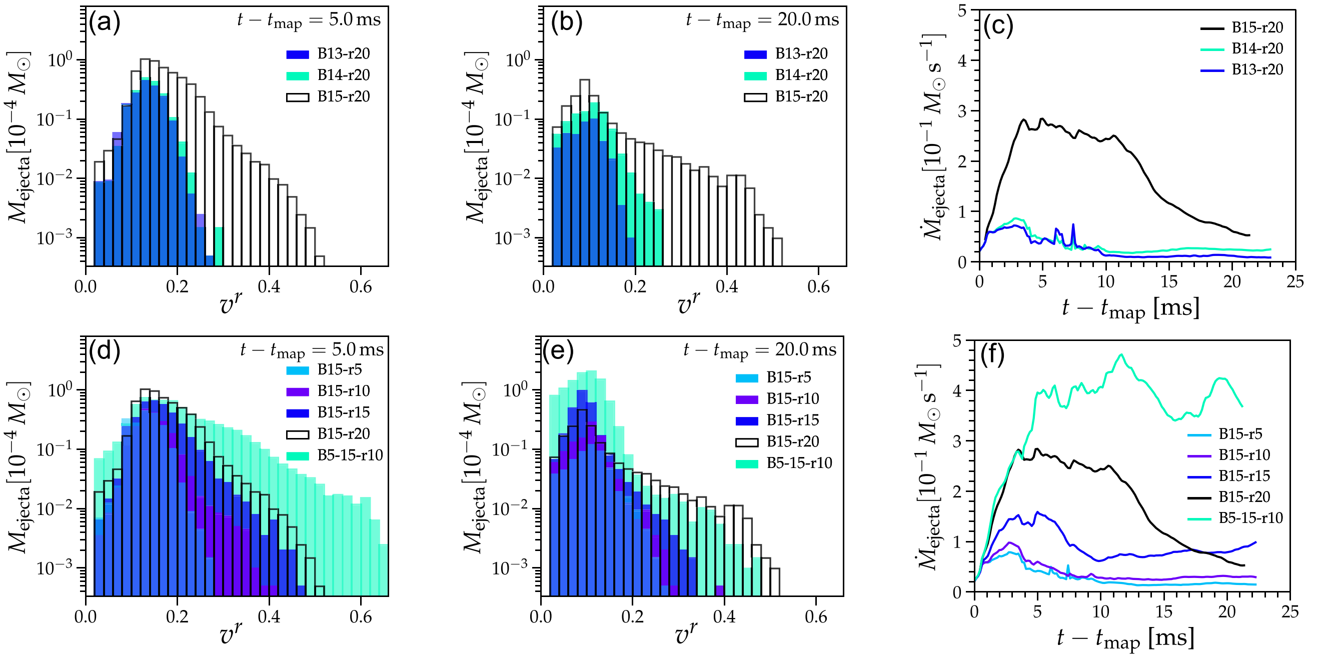

Figure 2. Panels a, b, and c: Comparison between simulations with various initial magnetic field strengths B_0, where we show B13-r20 in blue, B14-r20 in green, and B15-r20 in black. In panels a and b, we show histograms of the radial velocity $v^{\rm r}$ of unbound material (defined as material satisfying the Bernoulli criterion $-hu_{\rm t} > 1$) with corresponding ejecta masses $M_{\rm ejecta}$ at $t - t_{\rm map} = 5$ and 20 ms, where $t_{\rm map} = 17$ ms after coalescence. In panel c, we show the mass ejecta rate $\dot{M}_{\rm ejecta}$ of unbound material as a function of time. Panels d, e, and f: Comparison between simulations with different magnetic falloff parameter $r_{\rm falloff}$ (where B5-15-r10 is also included), where we show B15-r5 in cyan, B15-r10 in purple, B15-r15 in blue, B15-r20 in black, and B5-15-r10 in green. We show histograms of the radial velocity $v^{\rm r}$ of unbound material at $t - t_{\rm map} = 5$ and 20 ms in panels d and e and the mass ejecta rate $\dot{M}_{\rm ejecta}$ of unbound material as a function of time in panel f.

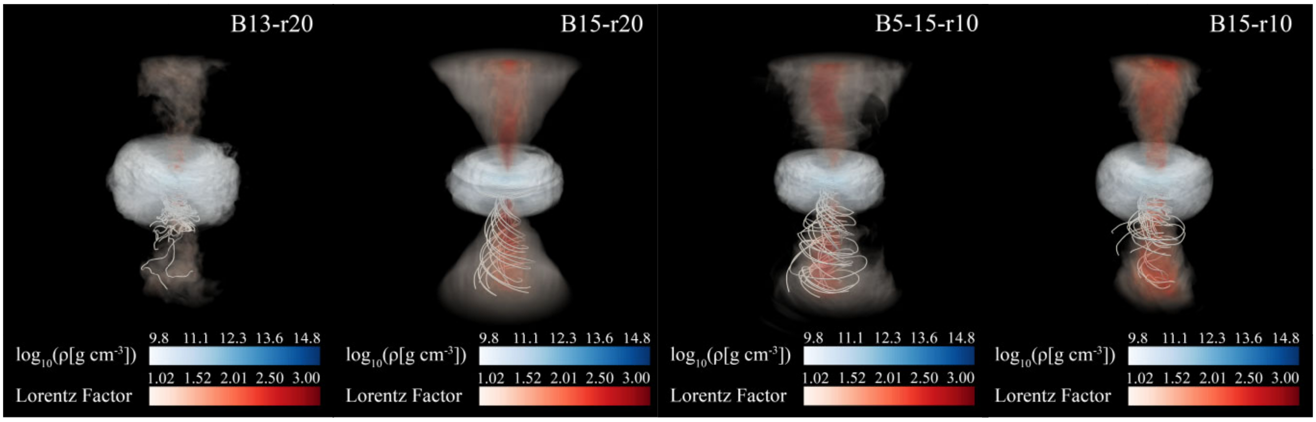

Figure 3. Volume renderings of the Lorentz factor (Bernoulli criterion) for the outflows (white-red colourmap) and density for the accretion torus (white-blue colourmap) of simulations B13-r20 (left), B15-r20 (middle-left), B5-15-r10 (middle-right), and B15-r10 (right) at $t - t_{\rm map} = 20$ ms, where $t_{\rm map} = 17$ ms after coalescence. The magnetic field lines are also shown in the lower plane ($z < 0$, where z is the vertical axis) in white. The top-to-bottom distance of the volume renderings is 355 km.

respectively, while B15-r5 only contains outflows with $v^{\rm r} < 0.28c$. At $t - t_{\rm map} = 20$ ms, the $v^{\rm r}$ profiles of simulations B15-r5, B15-r10, and B15-r15 look reasonably similar, where B15-r10 and B15-r15 have lost the majority of their high-velocity ($v^{\rm r} > 0.3c$) ejecta between $t - t_{\rm map} = 5$ and 20 ms. For B5-15-r10, nearly all $v^{\rm r} > 0.5c$ material has rapidly decreased or disappeared in the same time interval, although it has retained significant $M_{\rm ejecta}$ values in the $0.3c < v^{\rm r} < 0.5c$ regime. Simulation B15-r20, by contrast, displays larger high-velocity mass fractions at $t - t_{\rm map} = 20$ compared to $t - t_{\rm map} = 5$. Finally, we note that jetted outflow formation in simulations B15-r20 and B5-15-r10 leads to considerably larger $v^{\rm r}$ values compared to their purely magnetized wind-forming counterparts.

For the corresponding $\dot{M}_{\rm ejecta}$ panel, B5-15-r10 exhibits much larger $\dot{M}_{\rm ejecta}$ values compared to the other simulations including B15-r20, despite both simulations showing jetted outflow formation. Simulation B15-r20 does exhibit significantly larger mass ejecta rates throughout most of its evolution compared to B15-r15, B15-r10, and B15-r5. Furthermore, simulation B15-r15 exhibits considerably larger $\dot{M}_{\rm ejecta}$ compared to B15-r10 and B15-r5, even showing an increasing $\dot{M}_{\rm ejecta}$ trend towards the end of the simulation. Finally, simulation B15-r5 shows a very similar $\dot{M}_{\rm ejecta}$ evolution compared to B14-r20 and B13-r20, also displaying two short peaks at $t - t_{\rm map} \sim 6$ ms and $t - t_{\rm map} \sim 7.5$ ms.

In Fig. 3, we show volume renderings of the Bernoulli criterion (equivalent to the Lorentz factor) for the outflows (white-red colourmap) and density for the accretion torus (white-blue colourmap) of simulations B13-r20, B15-r20, B5-15-r10, and B15-r10 at $t - t_{\rm map} = 20$ ms. The magnetic field lines are also shown in the lower plane ($z < 0$, where z is the vertical axis) in white. When comparing B13-r20 and B15-r20, the latter shows a more structured accretion torus and a considerably larger amount of ejecta, in addition to higher Lorentz factors. Simulation B15-r10 shows a narrower outflow structure and relatively disordered magnetic field geometry compared to B15-r20, though notably contains similar Lorentz factors. Simulation B5-15-r10, despite forming jetted outflows, displays lower Lorentz factors when compared to B15-r20. The maximum Lorentz factor of B15-r20 is 3.94, whereas for B5-15-r10 it is 2.32. This is likely caused by the jet's radial velocities decreasing over time, as also implied by panels d and e of Fig. 2.

3.2 Evolution of the magnetic field

In Fig. 4, we show streamplots in the meridional (xz) plane of the magnetic field (that is, integrating the $\{B_x, B_z\}$ components) for simulations B13-r20, B14-r20, and B15-r20 at $t - t_{\rm map} = 0$ and 20 ms. We adopt three different values for the magnetic field strength $|\vec{\boldsymbol{B}}|$ to highlight their normative features for each simulation. The $t - t_{\rm map} = 0$ magnetic vector field represents the initial ordered magnetic field, which we compute from the vector potential A in equation (7) with varying B_0 and $r_{\rm falloff} = 20$ for each of the simulations. Also for $t - t_{\rm map} = 0$, at the surface of the star (depicted by the red line) and along the rotation axis, the magnetic field strength is $B = 7.6 \times 10^{12}, 7.6 \times 10^{13}, 7.6 \times 10^{14}$ G, for simulations B13-r20, B14-r20, and B15-r20, respectively. For $t - t_{\rm map} = 20$ ms, we compute the figures using simulation data, specifically from magnetic variables in the GRMHD evolution of the HMNS system. We infer the relation between the magnetic field parameters and its final configuration by comparing the magnetic field structure at early and late times. This is especially apparent for simulations B13-r20 and B14-r20, which show extreme changes in the magnetic field morphology between $t - t_{\rm map} = 0$ and 20 ms due to the field's adaptation to the underlying magnetohydrodynamical flow of the remnant system, thereby rapidly losing their large-scale structure. For simulation B15-r20, the field appears to be collimated in the polar region due to the development of large toroidal field components, seen in Fig. 3.

In Fig. 5, similarly, we show streamplots in the meridional (xz) plane of the magnetic field for simulations B15-r5, B15-r10, B15-r15, and B5-15-r10. The $t - t_{\rm map} = 0$ magnetic vector fields display the initial magnetic field computed from the vector potential A in equation (7) with varying $r_{\rm falloff}$ (and B_0 for B5-15-r10) for each of the simulations. Again for $t - t_{\rm map} = 0$, at the surface of the star (depicted by the red line) and along the rotation axis the magnetic field strength is $B = 4.7 \times 10^{13}, 2.8 \times 10^{14}, 5.7 \times 10^{14}, 1.4 \times 10^{15}$ G for simulations B15-r5, B15-r10, B15-r15, and B5-15-r10, respectively. All simulations, as before, adjust rapidly to the underlying magnetohydrodynamical flow, while showing different magnetic field morphologies and strengths throughout the displayed planes. For simulation B15-r5 at $t - t_{\rm map} = 20$ ms, the magnetic field is dominated by relatively low-$|\vec{\boldsymbol{B}}|$ values and disordered field configurations. Simulations B15-r10 and B15-r15, by contrast, display larger magnetic field strengths and higher degrees of order in their field structures, albeit also exhibiting disordered and/or low-$|\vec{\boldsymbol{B}}|$ regions. Simulation B5-15-r10 exhibits the most ordered field in combination with high-$|\vec{\boldsymbol{B}}|$ regions, although notably showing a considerably different field morphology compared to B15-r20 in Fig. 4.

Using the surface of the star as the reference for the magnetic field, simulations B15-r10, B15-r15, and B15-r20 have roughly the same order-of-magnitude field strength, namely $B = 2.8 \times 10^{14}, 5.7 \times 10^{14}$, and 7.6×10^{14} G, respectively. As the falloff parameter increases, we observe that the final configuration smoothly transitions from a magnetized wind to a collimated jetted outflow. The magnetic field strength at the surface of the star plays a fundamental role in the development of a collimated structure, however, the falloff parameter $r_{\rm falloff}$ which controls how much the magnetic field seeps out from the star also has an impact in shaping the HMNS outflow. In B15-r10, the initial strong magnetic field leads to a somewhat ordered configuration but without enough collimation nor strength throughout; conversely, B15-r20 with a larger falloff parameter allows the field to seep out of the star and leads to a collimated jetted outflow configuration. It is evident from the simulations considered here that low magnetic field strengths at the surface of the star with small falloff parameters lead to magnetized winds; however, high magnetic field strengths at the surface of the star with large falloff parameters develop jetted outflows within the time-scale of the simulations. Transitioning from one extremal final configuration to the other can be done smoothly varying these two parameters, as shown in Figs 4 and 5. In fact, B15-r15 shows signs of a large-scale ordering with strong magnetic fields throughout the simulation domain but without a strong collimation; this final configuration seems to be lying between the magnetized winds and jetted outflows.

3.3 Nucleosynthesis and kilonovae

In panel a of Fig. 6, we show electron fraction histograms of all tracer particles for simulations B13-r20, B14-r20, and B15-r20, when the temperature of the particles is last above 5 GK. As this is approximately the temperature at which r-process nucleosynthesis starts, the electron fractions at this temperature are the relevant quantities for setting the r-process yields. As mentioned, the approximate neutrino scheme of the simulations causes uncertainties in our nucleosynthesis predictions, where the r-process production of heavy elements may be reduced by up to a factor of $\sim$10 (when comparing the most extreme cases; Curtis et al. 2022). We compute the $Y_{\rm e}$ distributions using `SkyNet` (Lippuner & Roberts 2017). All simulations exhibit wide distributions in $Y_{\rm e}$, where especially B13-r20 contains more low-$Y_{\rm e}$ material while also showing some ejecta in the $0.1 < Y_{\rm e} < 0.16$ range. Simulation B14-r20 contains significant $Y_{\rm e} > 0.4$ ejecta, while also displaying a larger average $Y_{\rm e}$ compared to B13-r20. For B15-r20, a large amount of $0.24 < Y_{\rm e} < 0.34$ material is ejected, while also showing significant high-$Y_{\rm e}$ material. These results seem to tentatively imply that when increasing B_0, the $Y_{\rm e}$ of the ejecta generally shifts to larger values.

In panel b of Fig. 6, we show $Y_{\rm e}$ distributions of all tracer particles when their temperature is last above 5 GK for simulations B15-r5, B15-r10, B15-r15, B15-r20, and B5-15-r10. Simulation B15-r5 mostly contains ejecta with $Y_{\rm e} \sim 0.3$, albeit also showing both low- and high-$Y_{\rm e}$ material including an extremely low electron fraction at $0.1 < Y_{\rm e} < 0.12$. Simulations B15-r10 and B15-r15 mostly show ejecta around $Y_{\rm e} \sim 0.3$, although displaying significantly shallower distributions compared to the other simulations. Simulation B15-r20 contains similar ejecta masses compared to B15-r10 and B15-r15 around $Y_{\rm e} \sim 0.3$, although showing a considerably wider distribution.

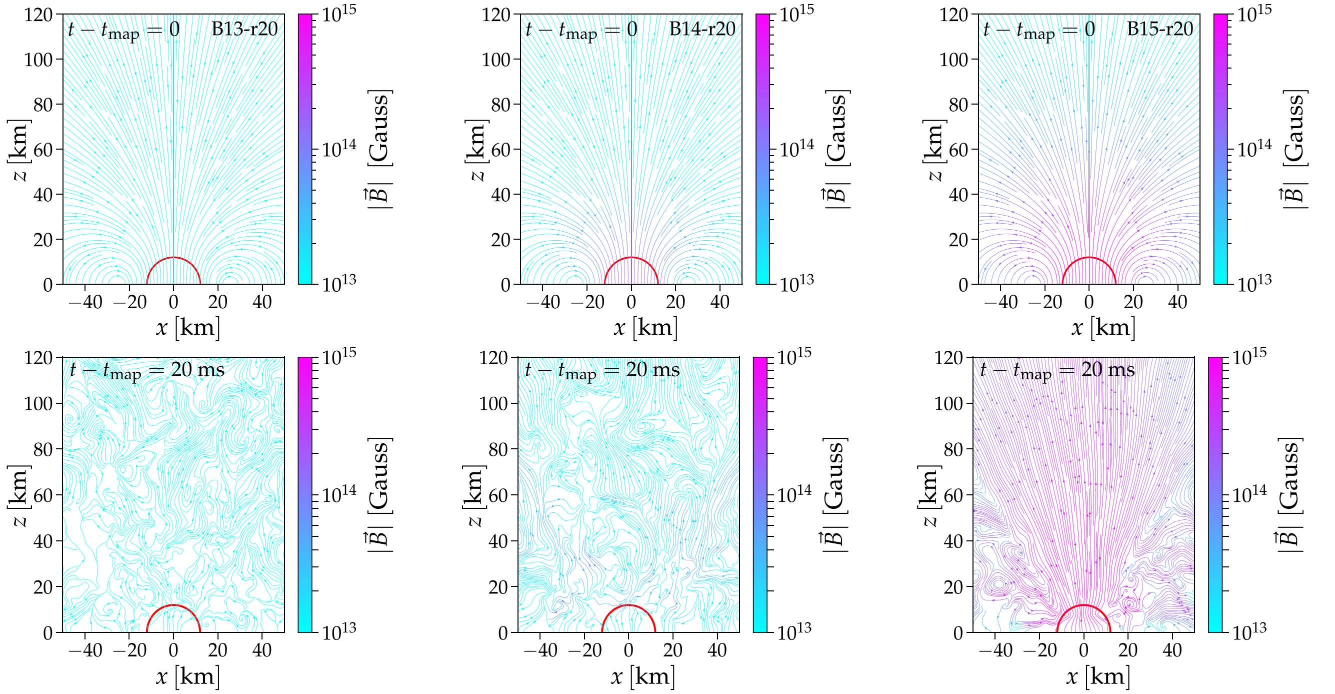

Figure 4. Streamplots of the magnetic field in the meridional (xz) plane (where z is the vertical axis) for simulations B13-r20, B14-r20, and B15-r20 at $t - t_{\mathrm{map}} = 0$ and 20 ms, where $t_{\mathrm{map}} = 17$ ms after coalescence. For $t - t_{\mathrm{map}} = 0$, we compute the magnetic field analytically using the vector potential A in equation (7) with varying B_0 for each of the displayed simulations. At the surface of the star, depicted by a red line, and along the rotation axis the magnetic field strength is $B = 7.6 \times 10^{12}, 7.6 \times 10^{13}, 7.6 \times 10^{14}$ G, for simulations B13-r20, B14-r20, and B15-r20, respectively, at $t - t_{\mathrm{map}} = 0$. For $t - t_{\mathrm{map}} = 20$ ms, we extract the magnetic field from the GRMHD simulations. Note the different limits used for the colourbars.

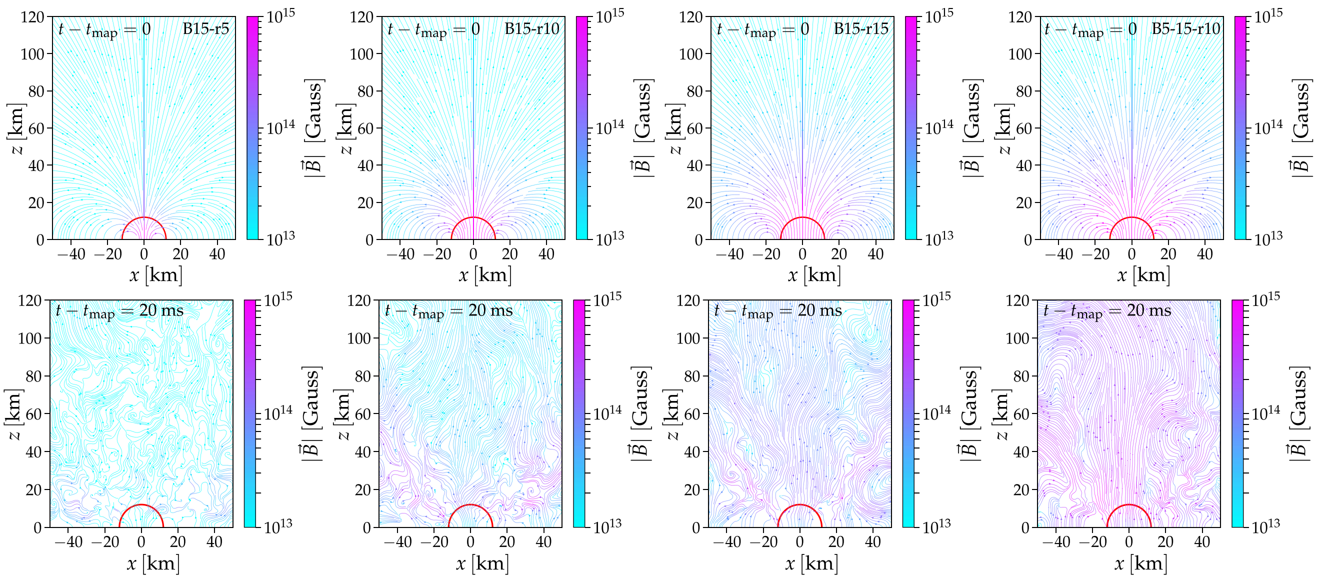

Figure 5. Streamplots of the magnetic field in the meridional (xz) plane (where z is the vertical axis) for simulations B15-r5, B15-r10, B15-r15, and B5-15-r10 at $t - t_{\mathrm{map}} = 0$ and 20 ms, where $t_{\mathrm{map}} = 17$ ms after coalescence. For $t - t_{\mathrm{map}} = 0$, we compute the magnetic field analytically using the vector potential A in equation (7) with varying r_{falloff} (and B_0 in the case of B5-15-r10) for each of the displayed simulations. At the surface of the star, depicted by a red line, and along the rotation axis the magnetic field strength is $B = 4.7 \times 10^{13},\ 2.8 \times 10^{14},\ 5.7 \times 10^{14},\ 1.4 \times 10^{15}$ G for simulations B15-r5, B15-r10, B15-r15, and B5-15-r10, respectively at $t - t_{\mathrm{map}} = 0$. For $t - t_{\mathrm{map}} = 20$ ms, we extract the magnetic field from the GRMHD simulations.

For B5-15-r10, a lower peak around $Y_{\mathrm{e}} \sim 0.24$ and significant low-Y_{e} ejecta of $Y_{\mathrm{e}} < 0.2$ is inferred. Although r_{falloff} comes in with a cubic power in equation (7), due to the astrophysically relevant small parameter range used, it is harder to discern a clear trend between r_{falloff} and Y_{e}. Indeed, some of the histograms have broadly similar features, which is to be expected given that the changes introduced through r_{falloff} are slightly more subtle. The differences in the Y_{e} distribution could arise due to the variation of the falloff parameter

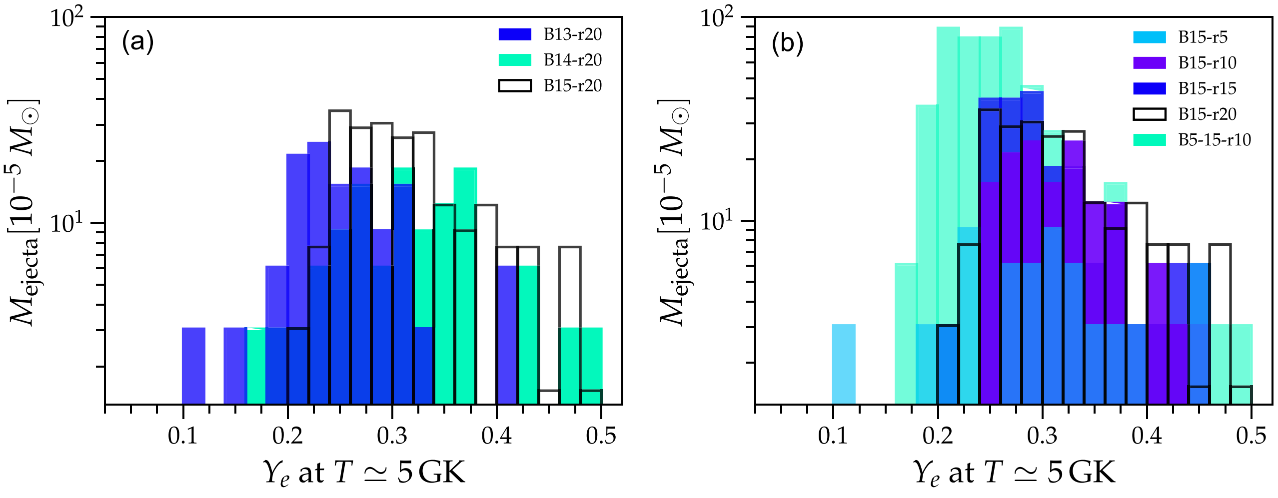

Figure 6. Panel a: $Y_{\rm e}$ histograms of all tracer particles for B13-r20 (blue), B14-r20 (green), and B15-r20 (black), when the temperature of the particles is last above 5 GK. We compute the $Y_{\rm e}$ distributions using `SkyNet`. Simulation B15-r20 is shown here and in panel b in black, as it is nearly identical to the lowest-resolution simulation of Mösta et al. (2020). Panel b: $Y_{\rm e}$ histograms of all tracer particles for B15-r5 (cyan), B15-r10 (purple), B15-r15 (blue), B15-r20 (black), and B5-15-r10 (green) when the temperature of the particles is last above 5 GK, which we again compute using `SkyNet`.

and/or differences in the flow structure that individual tracer particles advect along.

In panel a of Fig. 7, we show the fractional abundances as a function of mass number for simulations B13-r20, B14-r20, and B15-r20. We compute these abundances using the neutrino luminosity recorded by tracer particles for each simulation. As mentioned, the $Y_{\rm e}$ distributions (see Fig. 6) for each simulation should coincide with the inferred abundances, where $Y_{\rm e} \lesssim 0.2$ ejecta causes a strong *r*-process, $0.25 \lesssim Y_{\rm e} \lesssim 0.4$ results in unsubstantial amounts of heavy nuclei ($A > 140$) production and $Y_{\rm e} \gtrsim 0.4 - 0.5$ causes a weak *r*-process (Curtis et al. 2022). It is mainly interesting to investigate the amount of heavy nuclei production, for which B13-r20 shows the largest abundances for the majority of mass numbers. Simulation B14-r20 shows similar abundances in the heavy-nuclei regime, except in the range of $140 < A < 155$. For B15-r20, considerably lower amounts of heavy nuclei are produced for nearly all $A > 140$ regimes. The fractional abundances of these three simulations seem to be in line with the $Y_{\rm e}$ distributions in panel a of Fig. 6, as a larger B_0 leads to a decrease in heavy element production.

In panel b of Fig. 7, we show the fractional abundances as a function of mass number for simulations B15-r5, B15-r10, B15-r15, B15-r20, and B5-15-r10. We compute the abundances using the neutrino luminosities encountered by tracer particles. Notably, B15-r5 and B5-15-r10 display very similar abundances for $A > 140$, while also producing the largest fractions of heavy elements when compared to the other simulations in this panel. Indeed, the ejected material for simulation B15-r5 is only sampled by a small amount of tracers particles, which give rise to an abundance computation based on relatively low statistics. This may impact the relative abundances tracers are probing. For B15-r20 and B15-r15, similar heavy nuclei production is inferred, albeit not forming significant amounts of $A > 140$ material. Simulation B15-r10 displays even less nuclei with $A > 140$, while its fractional abundance rapidly drops after $A \gtrsim 200$. The abundances and the $Y_{\rm e}$ distribution are correlated as we expected, however, a definitive trend between the abundances and $r_{\rm falloff}$ is hard to discern. This, similarly, could come down to the trajectories of tracer particles within each simulations or to the subtle impact of $r_{\rm falloff}$ on the outflow composition.

In Fig. 8, we show kilonova light curves in terms of the bolometric luminosities L for all simulations, which we compute using outflow properties extracted at a radius of $r = 100\,{\rm M}_\odot$. In panel a, we show the bolometric luminosities for simulations with varying B_0. Simulations B13-r20 and B14-r20 exhibit very similar light curves, where the latter shows a slightly brighter peak. Simulation B15-r20 contains significantly larger luminosity values throughout its evolution compared to B13-r20 and B14-r20.

In panel b of Fig. 8, we show the bolometric luminosities obtained at $r = 100\,{\rm M}_\odot$, in this case for simulations B15-r5, B15-r10, B15-r15, B15-r20, and B5-15-r10. The brightest kilonova is produced by B5-15-r10, which shows both the largest luminosity peak and consistently larger L compared to the other simulations, including B15-r20. For B15-r15 and B15-r20, very similar kilonova light curves and peak values are obtained. Simulations B15-r5 and B15-r10 also exhibit similar luminosity evolution, although the latter produces a significantly larger peak.

4 SUMMARY AND CONCLUSIONS

We have performed seven GRMHD simulations of an HMNS system with varying parametrized magnetic field strengths and configurations, to investigate its effects on the outflow properties, nucleosynthesis yields, and kilonova light curves. Our simulations include a neutrino treatment and tabulated, nuclear EOS.

Simulations B15-r20 and B5-15-r10, which contain the strongest magnetic fields, show the emergence of collimated, mildly relativistic jetted outflows as opposed to magnetized winds only. Jetted outflows can emerge in the simulations as a result of the strong magnetic fields in addition to the incorporation of neutrino effects, as this reduces baryon pollution in the polar regions (e.g. Mösta et al. 2020). The jetted outflows are then collimated by hoop stresses from the strong toroidal magnetic field windup along the rotation axis of the remnant. For B5-15-r10 and B15-r20, we find multiple indications for the presence of mildly relativistic jetted outflows. Most notably, these two simulations exhibit larger velocities of unbound material and mass ejecta rates (see Fig. 2) compared to the other simulations. Finally, the magnetic field morphologies are more structured in the polar region, pointing towards jetted outflows (see Figs 3, 4, and 5).

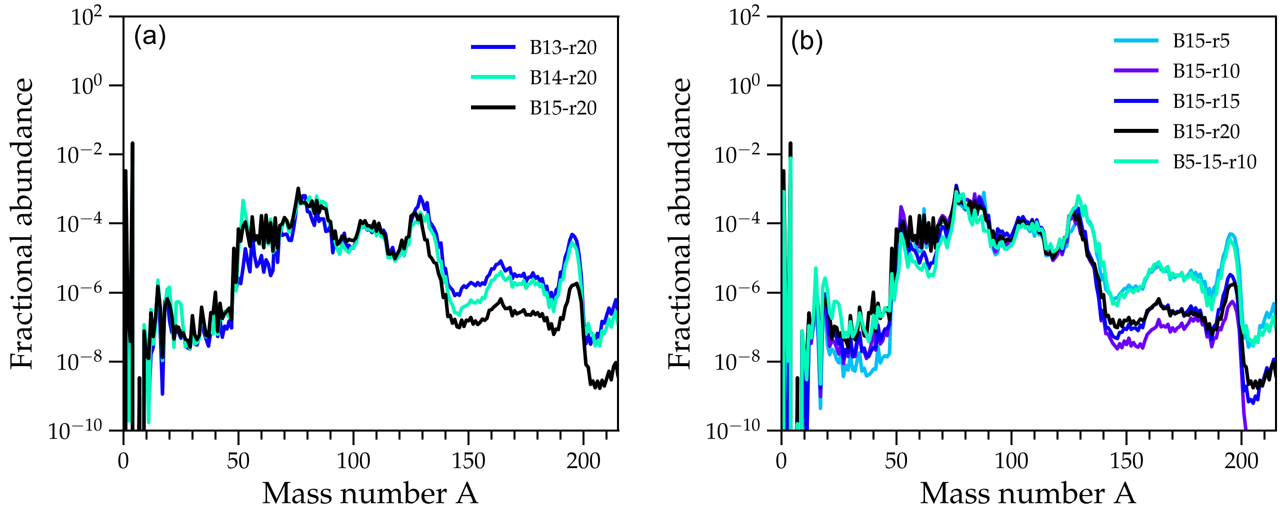

Figure 7. Panel a: Fractional abundances versus mass number for simulations B13-r20 (blue), B14-r20 (green), and B15-r20 (black), which we compute using the recorded neutrino luminosities of tracer particles. Simulation B15-r20 is shown here and in panel b in black, as it is nearly identical to the lowest-resolution simulation of Mösta et al. (2020). Panel b: Fractional abundances versus mass number for simulations B15-r5 (cyan), B15-r10 (purple), B15-r15 (blue), B15-r20 (black), and B5-15-r10 (green), which we again compute using the encountered neutrino luminosities of tracer particles.

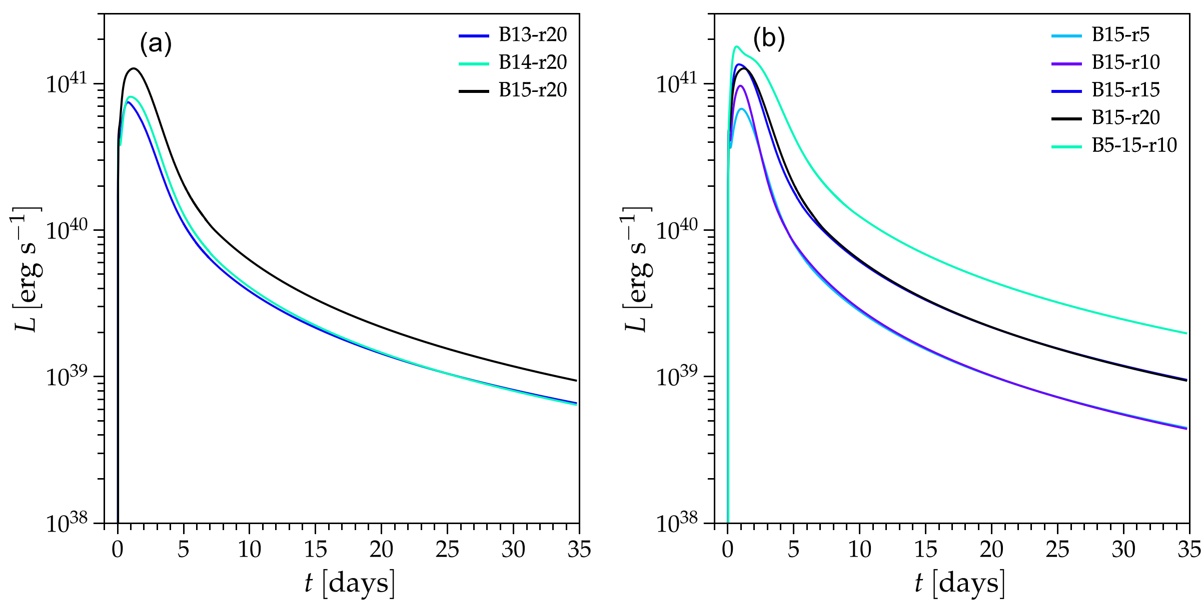

Figure 8. Panel a: Bolometric luminosity (computed at a distance $r = 100\,\mathrm{M}_{\odot}$) as a function of time for simulations B13-r20 (blue), B14-r20 (green), and B15-r20 (black). Simulation B15-r20 is shown here and in panel b in black, as it is nearly identical to the lowest-resolution simulation of Mösta et al. (2020). Panel b: Bolometric luminosity (computed at a distance $r = 100\,\mathrm{M}_{\odot}$) as a function of time for simulations B15-r5 (cyan), B15-r10 (purple), B15-r15 (blue), B15-r20 (black), and B5-15-r10 (green).

Additionally, the earlier collapse times of B5-15-r10 and B15-r20 (by ∼1.6 ms, see Fig. 1) indicate that angular momentum is more efficiently redistributed in the HMNS system.

In order to estimate the total ejected mass during the simulations, we integrate the mass ejecta rate over the phase of quasi-steady state evolution. Subsequently, we multiply by the total simulation time over the time of quasi-steady state evolution, to account for the HMNS system's full evolution. We choose to integrate over the phase of quasi-steady state evolution only to exclude variable mass ejecta rate behaviour in the early stages of the simulation. The quasi-steady state phase for $\dot{M}_{\mathrm{ejecta}}$ is different for each simulation (see panels a and b in Fig. 2), however, in all cases, we integrate from 10 ms up to the end of the simulation. This captures most or all of the quasi-steady state phase for the majority of simulations and allows for comparison between the estimated total ejecta masses, however, for B5-15-r10 and B15-r20 the integration interval is then (partly) over a non-quasi-steady state phase. We also compute the average of the mass ejecta rates over the same time interval. We list the results in Table 2 for all seven simulations. The averaged ejecta mass and mass ejecta rates for B5-15-r10 are considerably larger compared to all other simulations. This simulation, however, exhibits varying $\dot{M}_{\mathrm{ejecta}}$ behaviour throughout the evolution, meaning it does not reach a phase of quasi-steady state evolution before collapse. Despite simulations B15-r20 and B5-15-r10 both forming jetted

Table 2. Total ejecta mass $M_{\rm ejecta}$ and averaged mass ejecta rates $\dot{M}_{\rm ejecta}$ from the HMNS outflows. For all simulations, both values are computed from 10 ms up to the end of the simulation time.

Simulation	$M_{\rm ejecta}$ (10^{-4} M$_\odot$)	$\dot{M}_{\rm ejecta}$ (10^{-2} M$_\odot$ s^{-1})
B15-r20	26.8	12.7
B14-r20	5.2	2.3
B13-r20	2.4	1.1
B15-r5	3.4	1.6
B15-r10	6.1	2.8
B15-r15	17.1	7.8
B5-15-r10	83.1	39.8

outflows, we find much lower averaged $\dot{M}_{\rm ejecta}$ and $M_{\rm ejecta}$ values for the former, which is largely due to the $\dot{M}_{\rm ejecta}$ rapidly decreasing after $\sim$11 ms. The averaged ejecta values in combination with the $\dot{M}_{\rm ejecta}$ evolution and larger $v^{\rm r}$ velocities of unbound material for B5-15-r10 compared to B15-r20 (see Fig. 2) indicate that a considerably more powerful jetted outflow or magnetized wind emerges in the former simulation. Except for B15-r15, all other simulations show significantly lower averaged $\dot{M}_{\rm ejecta}$ and $M_{\rm ejecta}$ compared to the jet-forming simulations. However, as we infer $M_{\rm ejecta} > 10^{-4}$ M$_\odot$ for all simulations, even without jet-formation the contribution of ejected mass from the HMNS is relevant when compared to the dynamical ejecta, for which 10^{-4} M$_\odot$ $< M_{\rm ejecta} < 10^{-2}$ M$_\odot$ has been inferred (Hotokezaka et al. 2013). Furthermore, the results in Table 2 and Fig. 2 clearly show that for larger B_0 and $r_{\rm falloff}$, the mass ejecta and mass ejecta rates increase considerably. Similarly, the radial velocity of unbound material, shown in Fig. 2, increases significantly for larger values of the initial magnetic field parameters of the simulations.

By varying the magnetic field parameters, we probe different configurations of the HMNS system. As discussed, certain parameters lead to the formation of magnetized winds on the one hand, on the other they lead to formation of jetted outflows. However, there seems to be a continuous transition from one to the other. In fact, B15-r15 seems to be close to where the transition happens; its collapse time seems to be in line with the simulations that form magnetized winds (see Fig. 1), however in Fig. 5 we can see there is a collimated structure along the rotation axis. The magnetic field is not as strong as the cases where a jetted outflow is formed, and the mass ejecta rates and total ejecta masses are neither consistent with the jetted outflow nor the magnetized winds cases (see Table 2). Simulation B15-r15 suggests that by varying the magnetic field parameters one can go from the magnetized wind case to the jetted outflow smoothly.

Whether it is the magnetic field strength parameter B_0 or the physically relevant magnetic field strength at the surface of the star which shapes the HMNS outflow, it is clear that strong magnetic fields ease the development of jetted outflows, as shown in Figs 4 and 5. For this strong magnetic field to have some influence outside the star, within the time-scale of the simulation and before it collapses to a BH, it should seep out substantially. A larger falloff parameter $r_{\rm falloff}$, thus, is more conducive to collimated jetted outflows.

In the absence of jetted outflow formation, changing the $r_{\rm falloff}$ and B_0 parameters of the simulations has similar effects. Namely, these simulations exhibit remarkably similar collapse times, only showing marginal differences of $\sim$0.1–0.2 ms or less between simulations B13-r20, B14-r20, B15-r5, B15-r10, and B15-r15 (see Fig. 1). Also, they display reasonably similar mass ejecta rate evolutions (see panel a and b in Fig. 2). Such similarities could imply small magnetic field effects on outflow properties in the absence of jetted outflow formation. However, the magnetic field parameters have considerable effects on outflow properties for other quantities, also when jetted outflows are not formed. Firstly, the radial velocities of unbound material are significantly different between the five aforementioned simulations that do not form jetted outflows (see Fig. 2). Also, the $Y_{\rm e}$ distributions and fractional abundances show apparent dissimilarities. Another indication that the magnetic fields of these simulations have considerable effects on the outflow properties is that the averaged mass ejecta rates and total ejecta mass for these simulations are significantly larger compared to the purely hydrodynamical case without magnetic field, which has been conducted by Mösta et al. (2020; based on a nearly identical simulation code as this work). They find a total ejected mass of 5.8×10^{-5} M$_\odot$ and averaged mass ejecta rate of 2.4×10^{-3} M$_\odot$ s^{-1} during quasi-steady state evolution. Even the lowest values for both of these quantities from Table 2, for B13-r20, are a factor $\sim$4 and $\sim$4.5 larger for $M_{\rm ejecta}$ and $\dot{M}_{\rm ejecta}$, respectively.

The purely hydrodynamical simulation from Mösta et al. (2020) does show a very similar BH collapse time of $\sim$23 ms compared to the purely magnetized wind-forming simulations of this work. As mentioned, collapse times are partially dictated by the redistribution of angular momentum in the remnant system. Therefore, the similar collapse times of purely hydrodynamical and MHD simulations may imply that in the simulations forming magnetized winds the redistribution of angular momentum in the HMNS system is less efficient when compared to the simulations that form mildly relativistic jetted outflows.

Increasing B_0 by an order of magnitude seems to have significant effects on the $Y_{\rm e}$ distributions of the ejecta (when the temperature is last above 5 GK, see Fig. 6) and *r*-process yields (see Fig. 7). Namely, when increasing B_0, the $Y_{\rm e}$ distribution seems to shift to larger values while the fractional abundances exhibit lower amounts of heavy element production. Such a trend does not seem to exist for $r_{\rm falloff}$, which is especially clear when comparing the fractional abundances. However, as mentioned, this may caused by lower statistics for simulation B15-r5 (and possibly also B15-r10) due to a relatively low amount of tracer particles for this simulation, rather than being a consequence of a physical feature.

We have shown that the strength and specific configuration of the magnetic field in post-merger magnetars can lead to robust and sizeable effects in outflow properties, such as the mass ejecta rate and radial velocity of unbound material. Indeed, in two of the seven performed simulations, the larger values of the initial magnetic field strength and falloff result in the launching of mildly-relativistic jetted outflows, thus providing characteristic EM observables. Furthermore, the change in magnetic field parameters leads to profound effects on the abundance patterns and electron fractions, and hence on the kilonova light curves. We conclude, then, that the magnetic field strength and falloff have a significant imprint on the EM observables.

ACKNOWLEDGEMENTS

The authors thank Luciano Rezzolla for helpful discussions regarding magnetic field configurations on merger remnants and Roland Haas for his insights regarding technical aspects of the BlueWaters supercomputer. The simulations were carried out on NCSA's (National Center for Supercomputing Applications) BlueWaters under allocation ILL_baws, and TACC's (Texas Advanced Computing Center) Frontera under allocation DD FTA-Moesta. The analysis of the simulations was carried out on SurfSara's Spider under the allocation EINF-2585. This research was supported by the project CORTEX (Center for Optimal, Real-Time Machine Studies of the

Explosive Universe, NWA.1160.18.316) of the research programme NWA-ORC which is (partly) financed by the Dutch Research Council (NWO).

DATA AVAILABILITY

Simulation data are available upon reasonable request.

REFERENCES

Abbott B. P. et al., 2017a, ApJ, 848, L12
Abbott B. P. et al., 2017b, ApJ, 848, L13
Anderson M., Hirschmann E. W., Lehner L., Liebling S. L., Motl P. M., Neilsen D., Palenzuela C., Tohline J. E., 2008, Phys. Rev. Lett., 100, 191101
Brown D., Diener P., Sarbach O., Schnetter E., Tiglio M., 2009, Phys. Rev. D, 79, 044023
Chornock R. et al., 2017, ApJ, 848, L19
Ciolfi R., Kastaun W., Kalinani J. V., Giacomazzo B., 2019, Phys. Rev. D, 100, 023005
Cowan J. J., Sneden C., Lawler J. E., Aprahamian A., Wiescher M., Langanke K., Martínez-Pinedo G., Thielemann F.-K., 2021, Rev. Mod. Phys., 93, 015002
Curtis S., Mösta P., Wu Z., Radice D., Roberts L., Ricigliano G., Perego A., 2022, MNRAS, 518, 5313
Cyburt R. H. et al., 2010, ApJS, 189, 240
Dionysopoulou K., Alic D., Rezzolla L., 2015, Phys. Rev. D, 92, 084064
Einfeldt B., 1988, SIAM J. Numer. Anal., 25, 294
Fahlman S., Fernández R., 2018, ApJ, 869, L3
Foucart F., Mösta P., Ramirez T., Wright A. J., Darbha S., Kasen D., 2021, Phys. Rev. D, 104, 123010
Fuller G. M., Fowler W. A., Newman M. J., 1982, ApJS, 48, 279
Giacomazzo B., Rezzolla L., Baiotti L., 2009, MNRAS, 399, L164
Goriely S., Bauswein A., Janka H.-T., 2011, ApJ, 738, L32
Harten A., 1983, J. Comput. Phys., 49, 357
Hotokezaka K., Kiuchi K., Kyutoku K., Okawa H., Sekiguchi Y.-i., Shibata M., Taniguchi K., 2013, Phys. Rev. D, 87, 024001
Janka H.-T., 2001, A&A, 368, 527
Kasen D., Metzger B., Barnes J., Quataert E., Ramirez-Ruiz E., 2017, Nature, 551, 80
Kastaun W., Galeazzi F., 2015, Phys. Rev. D, 91, 064027
Kiuchi K., Cerdá-Durán P., Kyutoku K., Sekiguchi Y., Shibata M., 2015, Phys. Rev. D, 92, 124034
Kiuchi K., Kyutoku K., Sekiguchi Y., Shibata M., 2018, Phys. Rev. D, 97, 124039
Langanke K., Martínez-Pinedo G., 2000, Nucl. Phys. A., 673, 481
Lattimer J. M., Swesty D. F., 1991, Nucl. Phys. A., 535, 331
Lippuner J., Roberts L. F., 2017, ApJS, 233, 18
Liu Y. T., Shapiro S. L., Etienne Z. B., Taniguchi K., 2008, Phys. Rev. D, 78, 024012
Löffler F. et al., 2012, Class. Quant. Grav., 29, 115001
Margalit B., Metzger B. D., 2017, ApJ, 850, L19
Metzger B. D., 2017, preprint (arXiv:1710.05931)
Metzger B. D., Thompson T. A., Quataert E., 2018, ApJ, 856, 101
Morozova V., Piro A. L., Renzo M., Ott C. D., Clausen D., Couch S. M., Ellis J., Roberts L. F., 2015, ApJ, 814, 63
Mösta P. et al., 2014, Class. Quant. Grav., 31, 015005
Mösta P., Ott C. D., Radice D., Roberts L. F., Schnetter E., Haas R., 2015, Nature, 528, 376
Mösta P., Radice D., Haas R., Schnetter E., Bernuzzi S., 2020, ApJ, 901, L37
Nedora V., Bernuzzi S., Radice D., Perego A., Endrizzi A., Ortiz N., 2019, ApJ, 886, L30
Nicholl M. et al., 2017, ApJ, 848, L18
O'Connor E., Ott C. D., 2010, Class. Quant. Grav., 27, 114103
Oda T., Hino M., Muto K., Takahara M., Sato K., 1994, At. Data Nucl. Data Tables, 56, 231
Ott C. D., Burrows A., Dessart L., Livne E., 2008, ApJ, 685, 1069
Ott C. D. et al., 2013, ApJ, 768, 115
Pian E. et al., 2017, Nature, 551, 67
Radice D., Perego A., Hotokezaka K., Fromm S. A., Bernuzzi S., Roberts L. F., 2018, ApJ, 869, 130
Raynaud R., Guilet J., Janka H.-T., Gastine T., 2020, Sci. Adv., 6, eaay2732
Reisswig C., Ott C. D., Sperhake U., Schnetter E., 2011, Phys. Rev. D, 83, 064008
Reisswig C., Haas R., Ott C. D., Abdikamalov E., Mösta P., Pollney D., Schnetter E., 2013, Phys. Rev. D, 87, 064023
Rosswog S., Liebendörfer M., 2003, MNRAS, 342, 673
Ruffert M., Janka H.-T., Schaefer G., 1996, A&A, 311, 532
Savchenko V. et al., 2017, ApJ, 848, L15
Schnetter E., Hawley S. H., Hawke I., 2004, Class. Quant. Grav., 21, 1465
Shappee B. J. et al., 2017, Science, 358, 1574
Shibata M., Fujibayashi S., Hotokezaka K., Kiuchi K., Kyutoku K., Sekiguchi Y., Tanaka M., 2017, Phys. Rev. D, 96, 123012
Siegel D. M., Ciolfi R., Rezzolla L., 2014, ApJ, 785, L6
Smartt S. J. et al., 2017, Nature, 551, 75
Tanvir N. R. et al., 2017, ApJ, 848, L27
Tchekhovskoy A., McKinney J. C., Narayan R., 2007, MNRAS, 379, 469
Thompson T. A., Chang P., Quataert E., 2004, ApJ, 611, 380
Villar V. A. et al., 2017, ApJ, 851, L21
Zrake J., MacFadyen A. I., 2013, ApJ, 769, L29

This paper has been typeset from a TEX/LATEX file prepared by the author.